A rate-of-rise facility for measuring properties of wick structures

OPEN ACCESS
IOP Publishing
Measurement Science and Technology
Meas. Sci. Technol. **34** (2023) 045301 (15pp)
https://doi.org/10.1088/1361-6501/acad1c

A rate-of-rise facility for measuring properties of wick structures

A Elkholy[1], J Durfee[2], J P Mooney[3], A J Robinson[3] and R Kempers[1,*]

[1] Department of Mechanical Engineering, York University, Toronto, Canada
[2] Magna International Inc., 337 Magna Drive, Aurora, Ontario, Canada
[3] Department of Mechanical & Manufacturing Engineering, Trinity College Dublin, Dublin, Ireland

E-mail: kempers@yorku.ca

Received 14 September 2022, revised 23 November 2022
Accepted for publication 20 December 2022
Published 11 January 2023

Abstract

This work details a mass rate-of-rise (mROR) apparatus and analysis method for the accurate and precise determination of capillary wick parameters: permeability, K, effective pore radius, r_{eff}, and porosity, ε. Three factors were examined: (a) the accuracy of the theoretical models and their curve-fitting approaches associated with the mROR technique, (b) the influence of the experimental procedure on repeatability, and (c) how the uncertainty of the experimental input parameters propagates through the data analysis procedure and compounds the overall uncertainty of the wick parameters (K and r_{eff}). Four models and fittings methods were investigated: the Lucas–Washburn method, the gravity-based dm/dt method, the gravity-based t–m method, and the gravity-based m–t method. It is demonstrated that the m–t method developed here shows the lowest error and, equally importantly, that it is free of user decisions in the context of 'data scrubbing' because the entire mROR data set is used in its raw form. To test accuracy and repeatability, a precision-controlled mROR apparatus is proposed. Experiments were performed for commercially available wicks. A robust Monte Carlo error analysis method was developed and applied to quantify the overall uncertainty in the wick parameters as a function of the input uncertainties of all measured quantities.

Keywords: heat transfer, two-phase flow, heat pipes, wicks, porous structures, permeability, effective pore radius

(Some figures may appear in colour only in the online journal)

1. Introduction

Passive two-phase heat transfer devices, such as heat pipes and vapor chambers, are widely used in thermal management systems because of their passive operation, reliability, light weight, and high effective thermal conductivity. Porous metal capillary structures (wicks) are key components of heat pipes and vapor chambers because they provide the required capillary pressure to pump liquid from the condenser (heat sink) to the evaporator (heat source) region. As such, accurate characterization of wick parameters—in particular, the permeability, K, effective pore radius, r_{eff}, and porosity, ε—is crucial for modeling heat pipes and vapor chambers as well as designing passive two-phase thermal management systems.

Permeability is an intrinsic property of porous material that relates the flow rate to the resulting pressure drop. Together, the permeability, porosity, and pore radius, dictate the hydraulic performance of the wick. Several methods have been used to characterize the wick parameters separately, such as the bubble point [1] and the rising meniscus [2] methods for effective radius and the forced liquid flow method for

* Author to whom any correspondence should be addressed.

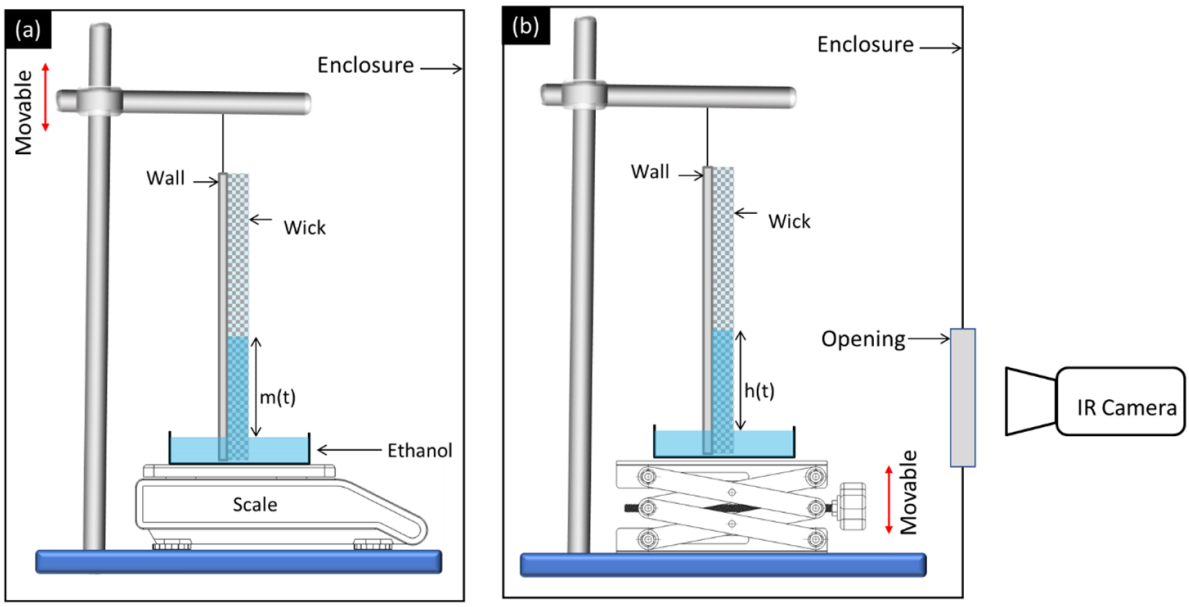

Figure 1. Wick hydraulic performance characterization methods: (a) mass rate-of-rise (mROR) method, (b) optical height rate-of-rise (hROR) method.

permeability [3–5]. However, the rate-of-rise (ROR) method is commonly used because it can determine both K and r_{eff} simultaneously from a single experiment. This method involves dipping the wick vertically into a liquid well (typically ethanol, acetone, or water) which then rises up within the wick under capillary action. The amount absorbed is tracked with time either directly, by measuring the mass of the fluid uptake with a load cell or scale (m–t technique, figure 1(a)), or indirectly, by visually monitoring the liquid front progress along the wick using an IR or optical camera (h–t technique, figure 1(b)). To extract the wick parameters, the data is fitted to the appropriate theoretical models that govern capillary rise phenomena.

Several models exist for describing the rising meniscus in a porous medium, and these differ depending on which forces can be regarded as negligible in the momentum equation. Lucas [6] and Gardner [7] were the first to propose analytical models for the capillary rise phenomena; they assumed that the capillary pressure is balanced only by the viscous pressure drop. The second (and most popular) model is the gravity-based model which includes hydrostatic and viscous forces in balancing the capillary pressure [8, 9]. Several fitting approaches can be employed with these models to predict permeability and effective pore radius independently. However, for these approaches, the user must carefully choose the data set from the full ROR curve such that the data sections are appropriate for the force balance assumption embedded in the theoretical model [10]. This 'data scrubbing' raises questions about the reliability of the ROR method for predicting both parameters simultaneously and leads to difficulties when comparing wicks across different studies. Some studies propose that it is more appropriate to couple the ROR experiment with the forced liquid flow method to improve accuracy [3–5, 11, 12]. Here, the ROR method is used to determine the capillarity factor ($\Delta P_{\text{cap}}\ K$) and the forced liquid flow method is employed to predict the permeability (K). Additionally, a third experiment is then required for the measurement of wick porosity.

In addition to there being a variety governing equations and ways and times to apply them, there is also a lack of consistency regarding the experimental procedure for the ROR method. In the context of this being a measurement technique, there is often missing, incomplete, or inconsistent information regarding crucial testing steps, including (but not limited to) the immersion length, data scrubbing and/or smoothing procedure, repeatability, and uncertainty analysis. With regard to the latter, uncertainty analysis is typically addressed by anticipating the error in the height [4, 13, 14] or the mass [13, 15] without propagating errors of the measured quantities to K and r_{eff}. Other methods rely on experimental repeatability as a measure of confidence in the measured quantities [16] or comparing results with different fluids with similar surface tension and wetting properties [17]; however, these can be considered qualitative measures of confidence because they do not account for measurement uncertainty of the instrumentation.

Despite extensive use of the ROR method in the literature, at present there is no standardized experimental approach which includes instrumentation, a repeatable test procedure, data analysis method, and robust uncertainty analysis. It is the aim of this work to address these shortcomings by introducing a straightforward and consistent protocol, free from user judgment and intervention, for capillary ROR experiments. This includes a clear justification of the chosen data analysis method, a description of the apparatus and instrumentation, and an explanation of an uncertainty analysis procedure that propagates instrument measurement error onto the measured quantities.

2. ROR models and theoretical background

When a wick is held vertically and brought into contact with a quiescent pool of liquid, initially the liquid rises rapidly into the wick structure and subsequently decelerates as gravitational, frictional, inertial, and/or evaporation-induced forces increasingly act on the fluid. The momentum equation describing this fluid flow is complex and, as a result, several models have been developed which neglect some of these forces: specifically, (a) the Lucas–Washburn model [6, 7], (b) the gravity-based model [8, 9], and (c) the Fries evaporation-based model [17]. The Lucas–Washburn model [6, 7] assumes no evaporation, neglects the hydrostatic pressure at the start of the wicking process, and presumes that the capillary pressure is balanced only by viscous pressure drop. In this model it is assumed that the liquid travels with a uniform velocity, the wick is homogenous, and the viscous pressure loss in a porous medium is governed by Darcy's law. Thus, the momentum equation is simplified to

$$\frac{2\sigma}{r_{\text{eff}}} = \frac{\mu\varepsilon}{K} h \frac{\mathrm{d}h}{\mathrm{d}t} \tag{1}$$

where ε, K, and r_{eff} are the wick porosity, permeability, and effective pore radius of the wick, respectively. h and t are the liquid height and the wicking time, respectively. Finally, μ and σ are the liquid viscosity and surface tension, respectively. The first term on the left side of equation (1) represents the maximum capillary pressure obtained using the Young–Laplace equation. Rearranging and integrating equation (1) gives

$$h^2 = \frac{4\sigma K}{\varepsilon \mu r_{\text{eff}}} t. \tag{2}$$

This model can be represented in terms of the absorbed mass because,

$$m = \rho\, T\, W\, h\, \varepsilon \tag{3}$$

where T and W are the wick thickness and width, while ρ is the fluid density such that,

$$m^2 = 2A\, t \tag{4}$$

where

$$A = \frac{2\sigma K \varepsilon (TW\rho)^2}{\mu r_{\text{eff}}}. \tag{5}$$

In the mass method (m–t), the wick performance factor (K/r_{eff}) is obtained by plotting a linear relationship between m^2 and t in equation (4). The permeability and the effective pore radius are independently predicted by measuring the maximum achievable mass gain or height; this requires very long samples and may take several days [17].

Another widely used model is the gravity-based model [3, 4, 11, 13, 14, 18–21], which accounts for the gravitational force by adding further terms to equation (1) and the model is expressed in terms of the mass gain as

$$\frac{\mathrm{d}m}{\mathrm{d}t} = \frac{2\sigma K \varepsilon (TW\rho)^2}{\mu r_{\text{eff}}} \frac{1}{m} - \frac{K g T W \rho^2}{\mu} \tag{6}$$

or

$$\frac{\mathrm{d}m}{\mathrm{d}t} = \frac{A}{m} - B \tag{7}$$

where

$$B = \frac{K\, g\, T\, W \rho^2}{\mu}. \tag{8}$$

Typically in this model, three fitting approaches are used to determine the constants A and B. The technique most frequently used is to perform a linear fit of the measured data to equation (7) by setting $x = 1/m$, and $y = \mathrm{d}m/\mathrm{d}t$ (heretofore referred to as the $\mathrm{d}m/\mathrm{d}t$ method). The second approach is to integrate equation (7) in terms of $t(m)$, not $m(t)$, resulting in equation (9); this is referred to as the t–m method. Thus, constants A and B are predicted by carrying out a non-linear curve fit of the entire data set according to

$$t = -\frac{m}{B} - \frac{A}{B^2} \ln\left(1 - \frac{B\, m}{A}\right). \tag{9}$$

The third approach is very similar to the previous one; however, it integrates m as a function of t, yielding

$$m(t) = \frac{A}{B}\left[1 + W\left(-e^{-1 - \frac{B^2 t}{A}}\right)\right] \tag{10}$$

where, W is the Lambert W function [22]. This method is heretofore referred to as the m–t method. Functionally, the t–m and m–t methods require that a non-linear regression analysis be performed to fit the analytic curve to the experimental data, resulting in predictions of A and B. If ε is known from a separate experiment, K and r_{eff} can then be calculated.

3. Experimental apparatus and methodology

3.1. Sample preparation

Wicks from three commercially available flat heat pipes (listed in table 1) were characterized experimentally using the ROR methodology and apparatus described herein. By carefully machining the edge material, two wick samples were extracted from each flat heat pipe and subsequently cut to a length of approximately 120 mm for testing. After machining, the wicks were cleaned in an ultrasonic bath of deionized water. Figure 2 shows photos of the wick samples before and after machining.

The width of each wick was measured at 12 different locations; these measurements are presented in table 1. The wicks were cross-sectioned at three locations along their length and imaged using a Leica MZ10 F stereomicroscope (figure 2); thus, it was possible to observe the uniformity of the sintered powder and measure the wick and base plate thicknesses, including their variability. The photos were thereafter analyzed using ImageJ software. The wick thickness was quite uniform, except in Wick 3 which had slight non-uniformity.

Table 1. Specifications of the wicks of the tested heat pipes.

	Heat pipe specifications			Measured dimensions		
Sample ID	Manufacturer	Part number	Heat pipe length (mm) X width (mm)	Base plate thickness, T_b (mm)	Wick thickness, T_w (mm)	Wick width, W_w (mm)
Wick 1	Wakefield-Vette	126218	500 × 16.85	0.585 ± 0.013	0.980 ± 0.02	13.81 ± 0.1
Wick 2	Advanced Thermal Solutions Inc.	ATS-HP-F8L150S38W-356	150 × 11.41	0.356 ± 0.01	0.59 ± 0.01	8.64 ± 0.12
Wick 3	Aavid, Thermal Division of Boyd Corporation	HP-CWS-F08x47-150-N	150 × 10	0.612 ± 0.01	0.69 ± 0.06	5.07 ± 0.2

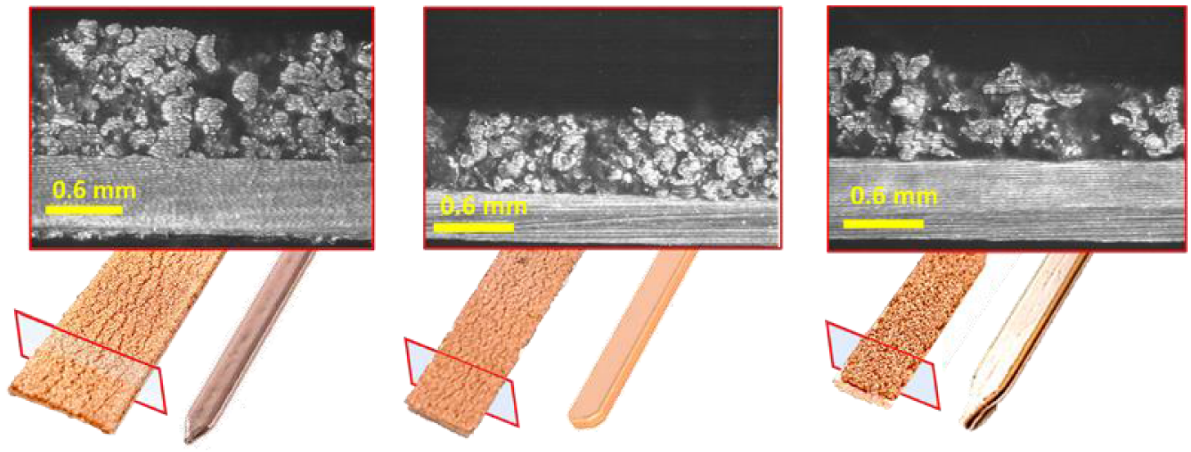

(a) (b) (c)

Figure 2. Microscopic cross-section and macro photo of each wick and heat pipe before and after sectioning: (a) wick 1, (b) wick 2, and (c) wick 3.

3.2. Apparatus description

Figure 3 shows a rendering of the mass rate-of-rise (mROR) apparatus, which consists of three main subsystems: (a) the capillarity testing section, (b) the computer-controlled mechanical gantry, and (c) the data acquisition system.

The test apparatus consists of a digital mass balance (Radwag AS 310.R2 PLUS) interfaced with a computer which records the real-time mass measurements at a sampling rate of 10 Hz. A 100 ml glass beaker containing 40 ml of ethanol was positioned on the balance. When the wick was dipped into the ethanol pool, the mass gain in the wick was measured by tracking the weight loss of the beaker placed on the balance. Evaporation from the ethanol pool and from the wick under test was minimized by fabricating a lid for the beaker with a slot just large enough to accommodate the sample, such that the open space was saturated with ethanol vapor [8]. In theory, the ROR method is not dependent on the fluid used. In practice, however, the most accurate results are obtained for highly wetting fluids which have a low volatility to limit errors induced by the rate of evaporation to the ambient. As such, ethanol is a popular choice because of its well-known properties, wetting characteristics, and relatively low volatility [11, 12, 14, 17].

The wick under test was orientated vertically on a fixture on a movable gantry which travels in the x and z directions. Movement can be precisely controlled using two stepper motors interfaced with a PC and control board. To mitigate the impact of ambient air movement on the balance reading, the whole assembly was sealed within an enclosure constructed from aluminum profile and acrylic sheets. The x-direction movement was used to position the sample over the beaker opening and allowed for the samples to be changed through a side door in the enclosure (not shown). The mechanical gantry was controlled in an open-loop configuration which controls the final position by either a set immersion depth or by measuring instantaneous contact between the wick sample and the liquid pool. The latter was accomplished by placing electrodes on the wick and in the liquid pool and measuring the electrical resistance (continuity) between them using an Agilent 34401A digital multimeter (DMM), as shown in figure 3 and explained in section 3.3. The gantry, the DMM, and lab scale were simultaneously controlled using a PC and in-house MATLAB script.

3.3. Experimental procedure

To perform the mROR test, the analytical balance was started and mass measurements were acquired for approximately 12 s before initiation of the wicking process. The wick sample was brought into contact with the working fluid by lowering it until

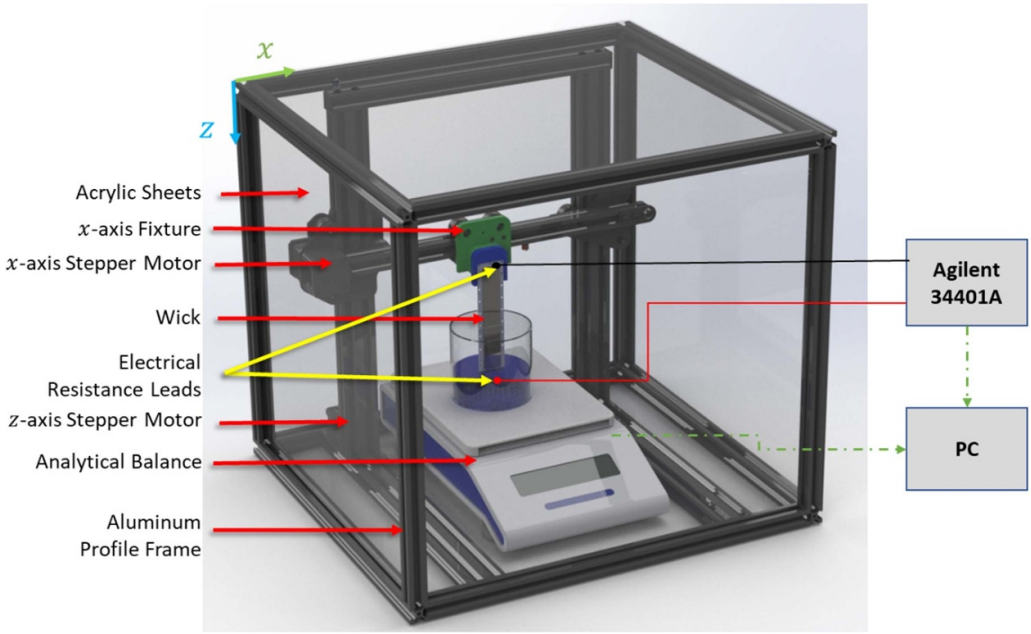

Figure 3. Rendering of the mROR facility developed in the current work.

the resistance measurement was triggered, ensuring a near-zero immersion length. The wick then remained in liquid contact and data was collected for 5 min, after which the wick was extracted from the pool. Then, another 60 s of data was collected to measure the mass gain of the meniscus, as explained in section 3.5.

3.4. Wick porosity measurement

The mROR method can produce a measurement of the constants A and B (section 2) by regression fitting of the chosen governing equation to the experimental data. However, this is not sufficient to isolate the desired parameters K, r_{eff}, and ε because they are grouped together in the constant B. Here, we propose a straightforward technique whereby a separate facility is not required to determine the porosity, and we subsequently verify this method against an established measurement method.

3.4.1. Combined m–t and h–t method. Height and mass versus time measurements were acquired to determine the experimental porosity of each sample wick (see table 5 in section 4.3). Figure 4 illustrates how the h–t and m–t techniques can be combined to determine porosity. To record the height of the liquid rising in the wicks, an IR thermal camera was placed in front of the enclosed apparatus, as per figure 4. A FLIR Thermacam™ P25 IR camera recorded 720 × 480 pixel high resolution full spectrum color images with a 30 Hz frame rate and real-time 12-bit data processing resolution and accuracy. The IR camera could accurately identify the front location based on the difference in emissivity between the liquid and sample material. Thus, the liquid wicking front, $h(t)$, and meniscus at the fluid reservoir, $h = 0$, were accurately identified and recorded.

Post-processing steps were applied to the images to measure the rise heights as a function of time. The time zero for the m–t and h–t data was matched so that each experimental time point had a corresponding height and mass value. When the wicks reach their maximum imbibition height, just prior to extraction from the pool, the height and mass can be used to calculate the porosity as

$$\varepsilon = \frac{m_{\max}}{\rho T W h_{\max}}. \tag{11}$$

The uncertainty of the porosity was based on the height error owing to the camera pixel resolution (±0.5 mm), mass error (±0.0012 g), and wick geometry variability. To ensure quality and repeatable results, the porosity measurements were taken three times for each wick and were found to be consistent to within about 2.5%, which is within the predicted measurement uncertainty.

3.4.2. Porosity verification—micro computed tomography. To verify the proposed experimental porosity measurement technique, x-ray computed tomography (XCT) was performed on the three test wicks. XCT can also be used in scenarios where it is cost prohibitive to utilize a high-resolution IR camera. XCT is a non-destructive methodology that can analyze concealed morphologies in 3D with fine resolution. Along with simple bulk properties like volume and area, it is possible to visualize and analyze porosity [23, 24], tortuosity [25], and pore and particle size distribution [26] using established processing techniques.

In this work, a Nikon XTH225ST with a 30–220 kV Tungsten x-ray source was used to acquire tomographic datasets of the sample wicks. A beam energy range of 120–140 kV was used, which corresponded to a practical resolution of ∼3 μm. The wicks were individually placed, in a vertical orientation,

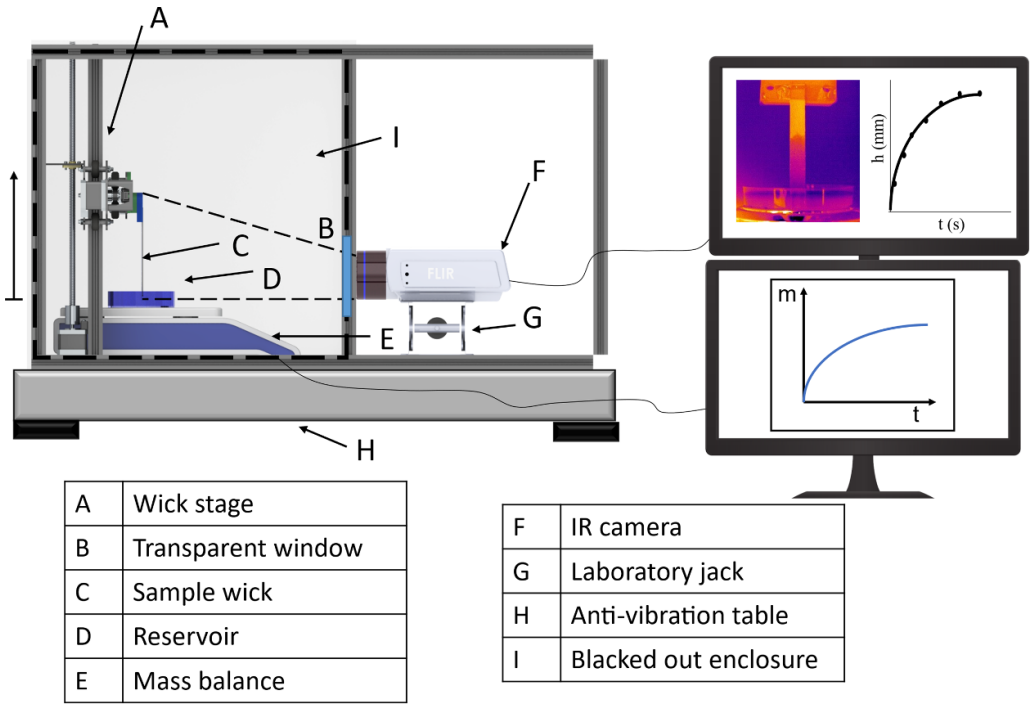

A	Wick stage
B	Transparent window
C	Sample wick
D	Reservoir
E	Mass balance

F	IR camera
G	Laboratory jack
H	Anti-vibration table
I	Blacked out enclosure

Figure 4. Schematic of the experimental height and mass-versus-time apparatus for determination of the wick sample porosity.

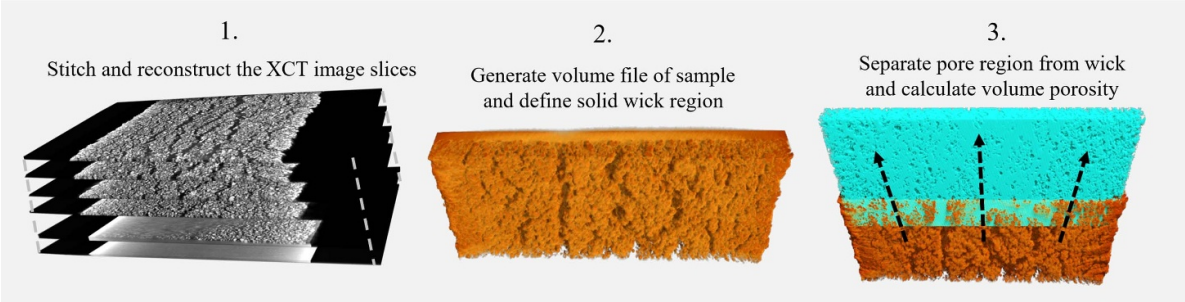

Figure 5. XCT procedure from image stitching to porosity analysis of the 3D-reconstructed wick. Here, the volume of low density (i.e. the pore space) was isolated using deep image segmentation tools, as described by Gobert *et al* [27].

inside the scanner. The wicks were then scanned at three locations over an axial distance of 15 mm that covered an image area of 15 mm^2; this is related to the distance of the sample from the x-ray source and the detector (du Plessis *et al* [23]). The stage rotated the wicks between the x-ray source and detector at a rate of 0.5° per image scan; 3000 line-of-sight images of the x-rays that passed through the samples were captured. Information on the effects of scan parameters on resolution is available elsewhere [27–29].

Figure 5 outlines the primary steps used to transform the XCT image stack to a 3D model and separate the wick, pore, and particle volumes to quantify porosity. The data sets were exported as a volume file that was then converted into a series of vertically aligned 2D greyscale tiff images. These images were used for image processing purposes. The current study utilizes the image processing platform developed by ORS Dragonfly (Object Research Systems 2018 [30]), and thus the following steps were applied to calculate porosity:

(a) The image stack was imported onto the ORS Dragonfly image processing platform and the image set dimensions were confirmed; this is normally pre-encoded from the x-ray microscope.
(b) It was confirmed that no artifacts were evident, and image filtering was applied to remove ambient noise identified inside the XCT scanner. The solid copper wick was isolated and registered as a 3D volume.
(c) The pore, particle, and wick regions of interest were defined by subtracting the base plate using historiographic image segmentation or deep learning image segmentation tools [27]. The volume for each region of interest for the porosity calculation was extracted.

Once these steps were conducted, the porosity of the wicks was calculated from the ratio of volumes, defined as

$$\varepsilon = \frac{V_{\text{pore}}}{V_{\text{wick}}} \tag{12}$$

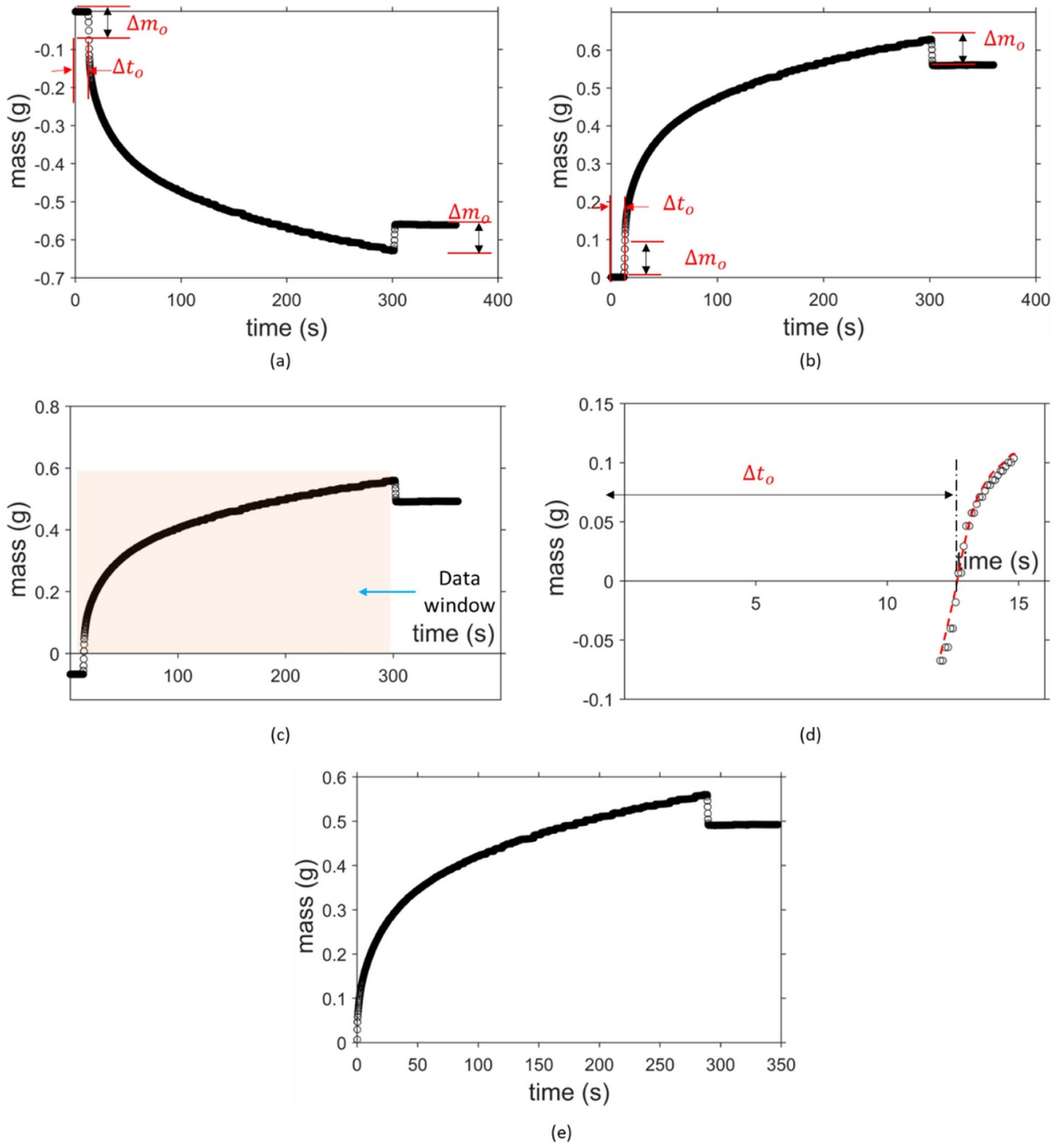

Figure 6. Data correction procedure: (a) weight loss measured by the lab scale; (b) equal and opposite mass uptake by the wick; (c) corrected data after subtracting the meniscus mass, Δm_0; (d) correction for the time lag, Δt_0; and (e) final corrected data.

where, V_{pore} and V_{wick} are the volume of the pore and wick regions, respectively. To ensure measurements represented the porosity of the entire homogeneous wicks, three scans were performed at three locations along the wick. The same x-ray conditions were applied for all scans, and the results for the three scans were averaged. For this method, it was found that the wicks were homogeneous with a maximum deviation in porosity of ± 0.025 ($<5\%$) between the scanned sections.

3.5. Data correction

Figure 6 shows the measured mROR data for Wick 1, where figure 6(a) is the actual weight loss measured by the precision scale and figure 6(b) is the corresponding mass uptake by the wick. The data was first corrected for (a) the additional mass associated with the initial wetting of the side meniscus (Δm_0), and (b) the time interval between the beginning of data sampling and the start of the wicking event (Δt_0).

When the wick first contacts the liquid, an attached meniscus is formed, after which the liquid wicks into the capillary structure. As shown in figure 6(b), this causes an immediate increase in the measured mass, Δm_0. To account for this effect, the mass of the meniscus is determined by extracting the wick at the end of the test period, causing the meniscus to detach. This results in a sudden drop in mass which is equivalent to the meniscus mass [8], as illustrated in figure 6(b).

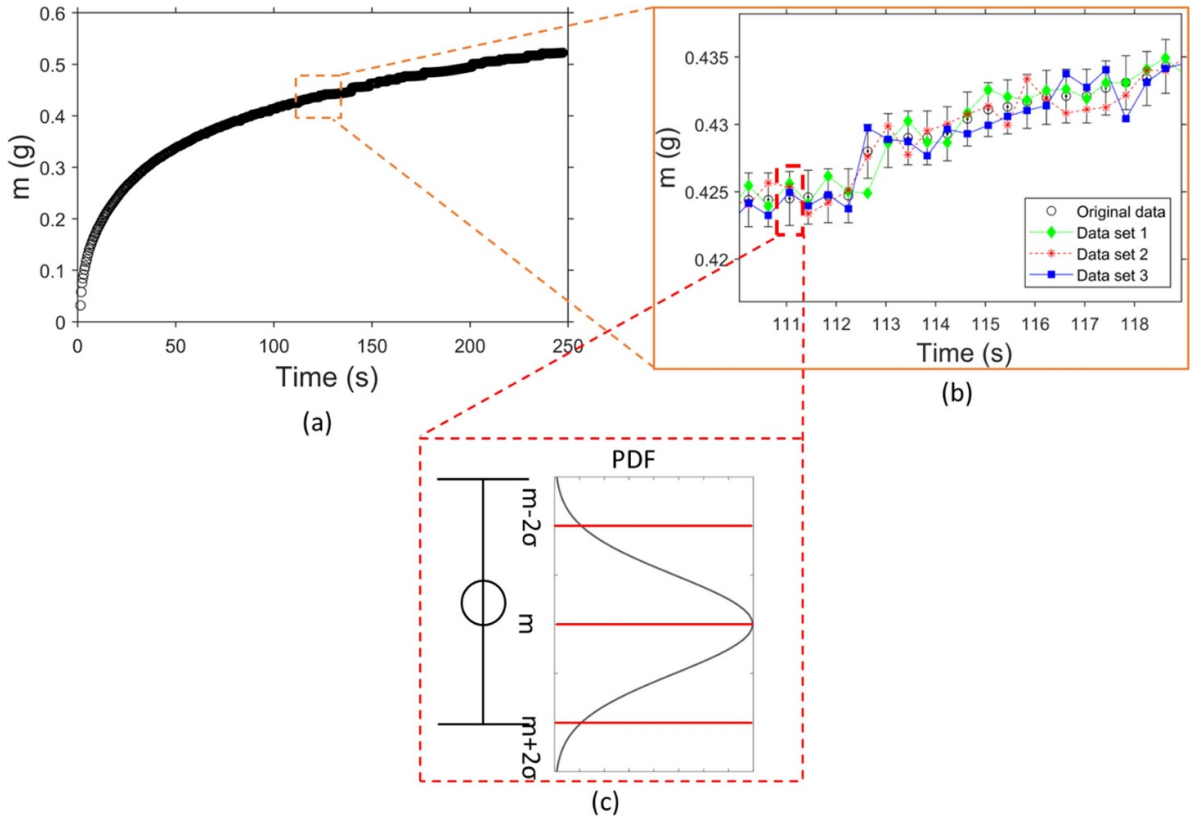

Figure 7. Data generation for the Monte Carlo simulation: (a) full data set, (b) close-up of the data range $110 < t < 120$, and (c) schematic representation of the normal probability distribution for m.

Figure 4(c) shows the meniscus-corrected mROR curve, which must now be adjusted for Δt_0; this is determined by calculating the root of a second-order polynomial regression fit to four data points on either side of the crossover point before wicking commences, as shown in figure 6(d). The time delay includes the time associated with the delay from the commencement of data sampling as well as the meniscus wetting time. Figure 6(e) shows the final mROR data for this example case.

3.6. Development of uncertainty technique

As discussed, the wick properties are obtained by performing a least squares regression of the measured mass to one of the models presented in section 2 to obtain the parameters A and B; these can then be used to extract the wick parameters, K and r_{eff}, based on the fluid properties, wick geometry, and measured porosity. As a result, the combined total uncertainty associated with the mROR technique depends on two elements: (a) the uncertainty associated with the model fitting parameters (A and B), and (b) the uncertainty of input parameters such as fluid properties, wick geometry, and porosity. The latter are relatively straightforward and are attained by establishing a confidence level for each input parameter. However, predicting the uncertainty of A and B is somewhat more complex because each data point of the experimental mROR curve has its own temporal and mass uncertainties, which are difficult to propagate through least squares regression. Historically, these uncertainties have not been considered.

The present work proposes a robust uncertainty method to accurately characterize K and r_{eff} independently using a Monte Carlo simulation method. The approach requires defining a 'confidence zone' for each data point based on the measurement uncertainty for mass, m. For this facility, the temporal uncertainty, t, was negligibly small, so it is omitted here; however, it can be easily incorporated if desired. Subsequently, all measurement points are simulated to move randomly with a normal distribution within each respective uncertainty range, as illustrated in figure 7, and the fitting parameters (A and B) were obtained using the non-linear least square regression fitting to the governing equation. A statistically sufficient number of randomized m versus t data sets are then generated by repeating the process thousands of times to generate normal distributions of A and B, where their respective standard deviations (2σ) reflect the propagated uncertainty of the mass measurement uncertainty of the scale.

The key temporal factor that affects the uncertainty of the fitting parameters A and B is the uncertainty of the time at which the wicking event started, Δt_0, defined in section 3.5. This was incorporated into the overall uncertainty determination by first running the Monte Carlo simulation at the nominal Δt_0, as discussed above, then re-running the simulation while randomly changing the Δt_0 a statistically sufficient number of times, with fixed mass data. The resulting total uncertainty in A or B is estimated as

$$\omega^2 = (\omega_{m-t})^2 + (\omega_{\Delta t_0})^2 \tag{13}$$

where ω_{m-t} accounts for the propagated uncertainty of the mass balance and $\omega_{\Delta t0}$ accounts for uncertainty in the calculated delay time.

4. Results & discussion

The results section begins by comparing the veracity of the different mROR models discussed in section 2. This was done for a hypothetical idealized wick, where the correct results were known *a priori*, to isolate the accuracy of the assessment method so that the most appropriate one could be selected with rigorous justification. Next, the effect of the immersion length, something not considered in the past, is discussed for one of test wicks. Finally, each test wick was experimentally examined using the selected model, immersion length, and the newly proposed uncertainty technique.

4.1. Accuracy evaluation of ROR models

One crucial task of the current work is to examine the accuracy of each potential mROR model outlined in section 2 and to assess their appropriateness for predicting K and r_{eff}. This was accomplished by using a hypothetical wick with known values of A and B. In this way, the model accuracy could be determined by inputting the wick properties beforehand, generating clean mROR data (using equations (9) or (10)) and subsequently applying the prediction model to re-extract the properties. The discrepancy between the input and output A and B (or equally K and r_{eff}) is indicative of the accuracy of the approach, quantified as

$$\text{Error}_A = \frac{A - A_{\text{input}}}{A_{\text{input}}}\,(\%), \text{Error}_B = \frac{B - B_{\text{input}}}{B_{\text{input}}}\,(\%) \qquad (14)$$

where, A_{input} and B_{input} are the input parameters of the hypothetical wick, calculated based on reasonable values of the geometrical and hydraulic properties reported by Feng *et al* [18] (see table 2). Figure 8 shows the generated idealized mROR curve based on A_{input} and B_{input}, hereafter referred to as the hypothetical wick.

4.1.1. Lucas–Washburn method. The accuracy of the Lucas–Washburn method was evaluated by plotting m^2 versus t using the hypothetical wick data, which is shown in figure 9(a). Here m^2 correlates linearly with t only during the early stages of imbibition when gravity forces are negligible (see figure 9(a) inset). When fitted to a straight line, the slope is equal to $2A$, according to equation (4). Figure 9(b) shows the expected error in the wick parameter A and the R^2 value of the obtained best fit line as a function of the time window used for regression fitting. The time window given is represented by the dimensionless time, $\tau = t/t_s$, where $t_s = 375.3$ s is the time required to reach 99% of the maximum absorbed mass, m_s. For instance, figure 9(a) inset shows the time window up to $t = 8$ s, giving $\tau = 0.021$ and an error of 20% despite $R^2 = 0.9946$. Clearly, the error is very sensitive to the sampling time window and produces unacceptable error, even with near-unity R^2 values. To achieve an error of less than 10%, $\tau \leqslant 0.0046$, which is only about 1.8 s of data-gathering time for this hypothetical wick. Overall, this method may be practical for certain families of porous material where the imbibition rate is comparatively slow, requiring higher ratios of A/B^2; however, it is not practical here, nor is it practical for typical wicks used in heat pipes and vapor chambers. Furthermore, the method does not estimate the parameter B, so it can only produce an estimate of the ratio K/r_{eff} unless the full mROR curve is produced which would allow it to be obtained from the steady-state data.

Practically, this method produces only one of the required parameters. In addition, relying on goodness of fit (R^2) [3, 19] as a confidence measure has been shown to be insufficient and can lead to a significant error. Furthermore, the Lucas–Washburn method only uses the initial linear portion of the mROR curve, which can be limited for practical wicks and influenced adversely by the meniscus attachment or the dynamic movement of the sample. Considering these limitations and the lack of guidelines and strict protocols around user judgments about data interrogation windows, range of applicability etc, it is not surprising that studies have reported significant deviation when comparing Lucas–Washburn predictions to other methods [5, 11]. For these reasons, this method is deemed inadequate.

4.1.2. The gravity-based (dm/dt) method. To implement the dm/dt method, the measured data comprising the mROR curve

Table 2. Assumed parameters of the hypothetical wick.

Parameter	Input value
Permeability, K	2.50×10^{-11} m^2
Porosity, ε	0.45
Effective radius, r_{eff}	150 μm
Wick thickness, T	0.7 mm
Wick width, W	7 mm
A	4.21×10^{-5} (g^2 s^{-1})
B	6.35×10^{-4} (g s^{-1})

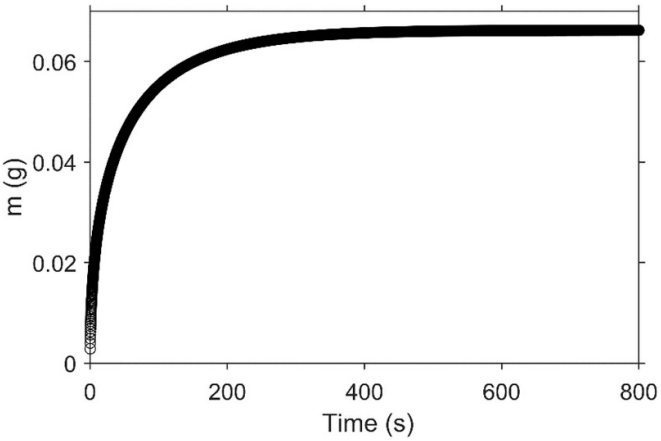

Figure 8. The generated mass data for a hypothetical wick with A $= 4.21 \times 10^{-5}$ (g^2 s^{-1}) and B $= 6.35 \times 10^{-4}$ (g s^{-1}).

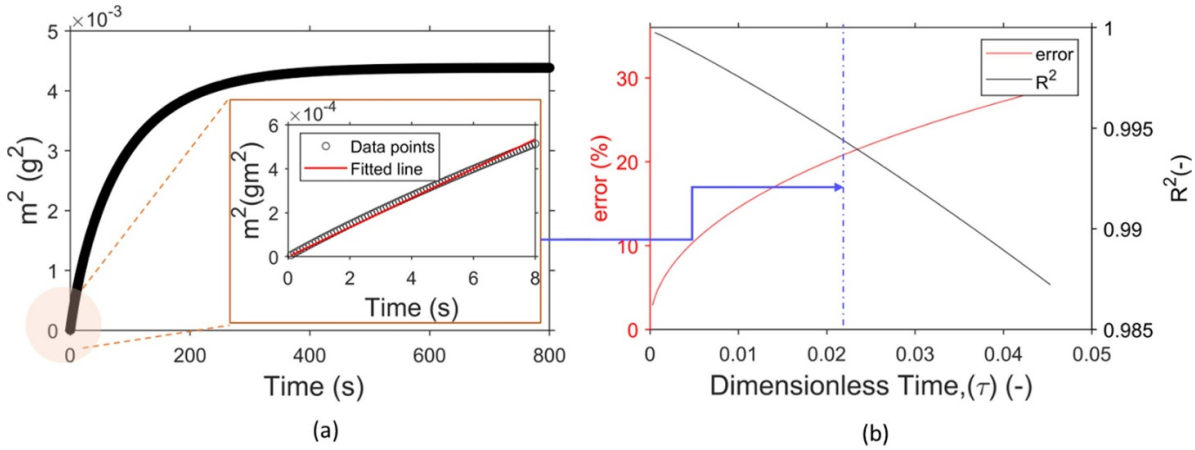

Figure 9. (a) Best fit line to the Lucas–Washburn model. (b) The error associated with this model.

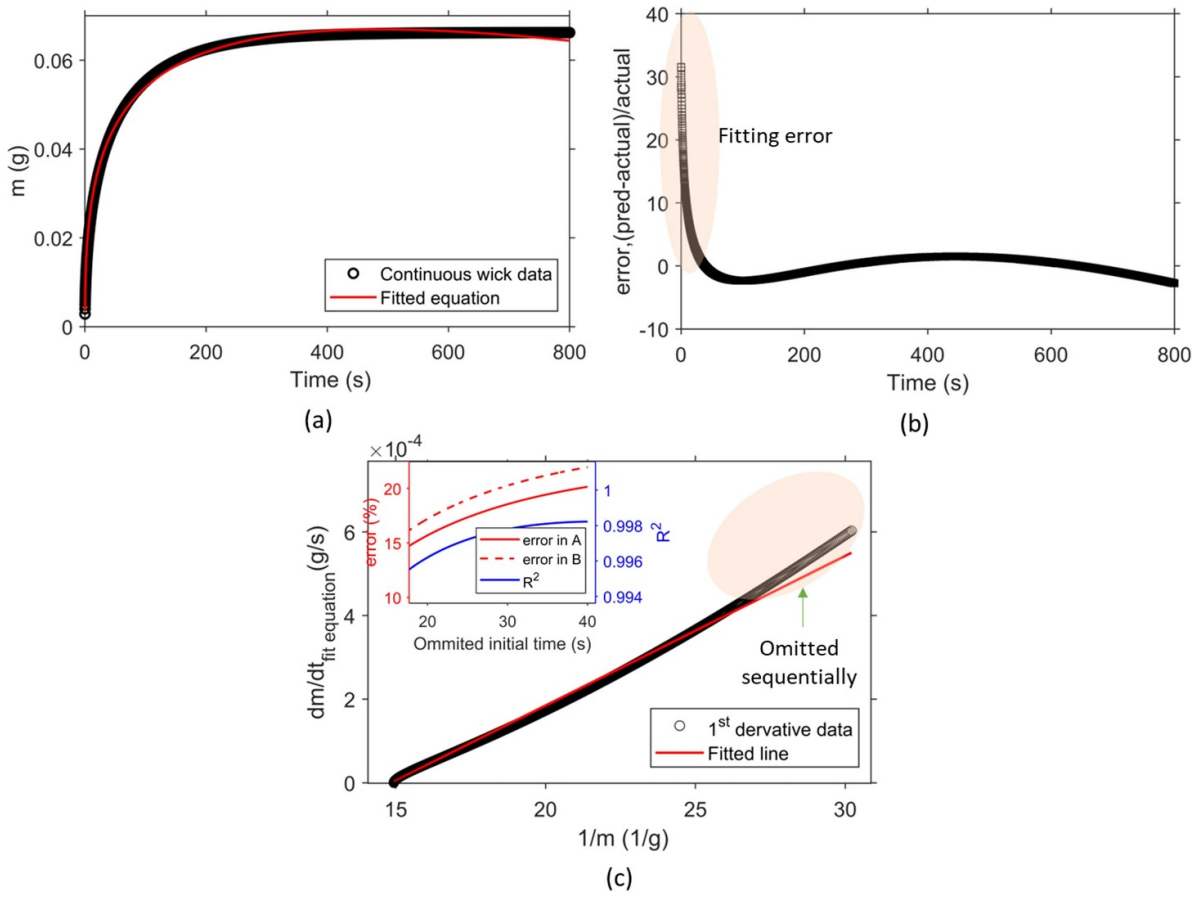

Figure 10. (a) Hypothetical wick data and its best fit function, (b) deviation of the best fit data from actual continuous input data and the associated error, (c) linear regression for the continuous data of the hypothetical wick, and (d) linear regression for the data obtained with the fit function and the associated error.

must first be approximated as a continuous function so that the time derivative of mass can be estimated. To illustrate this, the hypothetical wick data was fit to a power law function ($m(t) = a_0 + a_1 t^b + a_2 t^c$) with $R^2 = 0.989$, as depicted in figure 10(a). The functional form and goodness of fit of the fitting curve represents the first user decision in the process. As figure 10(b) illustrates, the agreement error is typically unacceptably large at early times (relative error $>5\%$) and must be omitted from the analysis, signifying a second potential user intervention. Subsequently, dm/dt versus m^{-1} is plotted (figure 10(c)) and a linear regression is performed so that the parameters A and B can be determined from the slope and vertical axis intercept (equation (7)). However, the linearity of the resulting curve is very sensitive to the curve-fitting process.

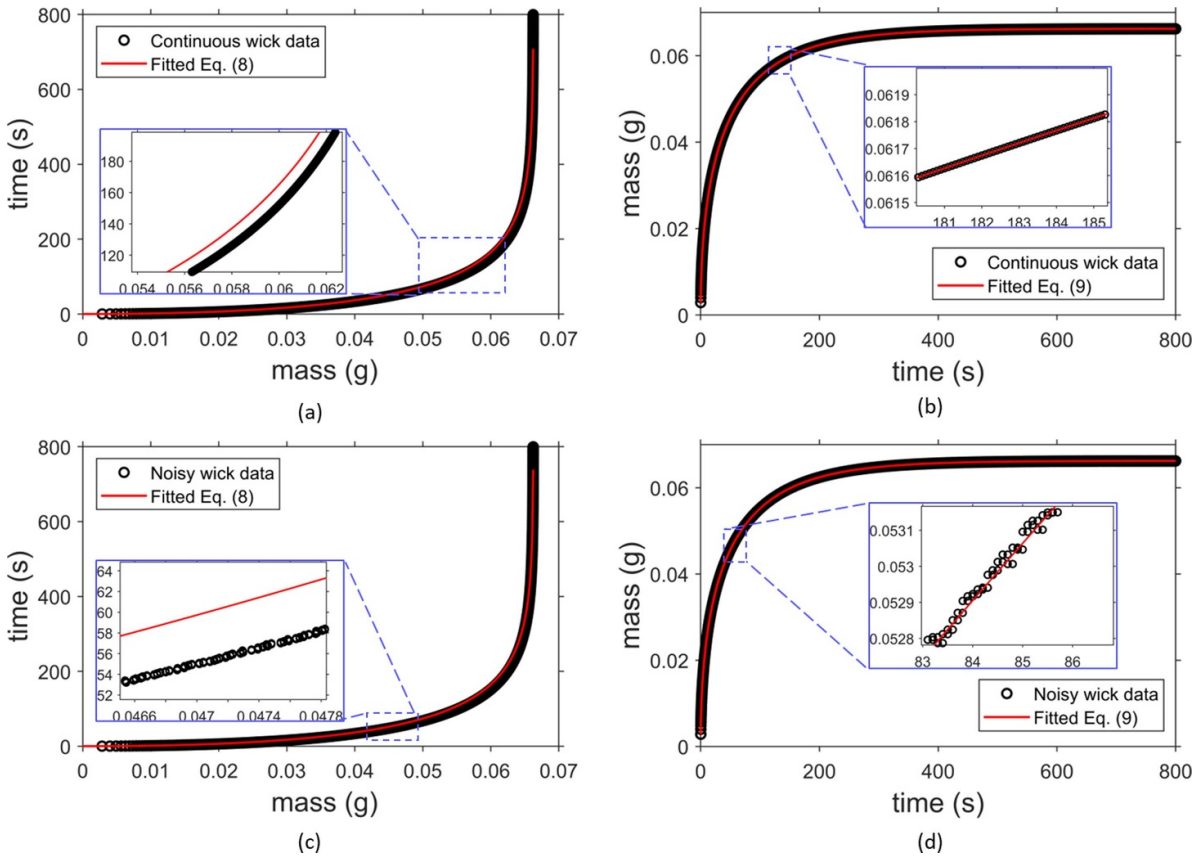

Figure 11. Fitting the hypothetical wick with (a) continuous data to the t–m method, (b) continuous data to the m–t method, (c) noisy data to the t–m method, and (d) noisy data to the m–t method.

Despite near-unity R^2 and elimination of unacceptably high fitting error data, some deviation from a straight line is inevitable owing to the high curvature of the initial mROR curve (figure 10(c)). This may suggest that a third user intervention is appropriate, where data points at higher or lower m^{-1} are omitted to maximize R^2, for example. However, as the inset plot of figure 10(c) shows, omitting higher m^{-1} (lower time) can have the opposite effect in terms of error on the predicted value of parameters; further, this is only exposed here because the values of A and B are known, which is not the case when implemented in a real situation. Overall, it is the opinion of the authors that the dm/dt method is inappropriate for a rigorous, consistently accurate, and procedure-orientated measurement method.

4.1.3. The gravity-based (t–m) and (m–t) models. Both the *t–m* and *m–t* approaches implement non-linear regression analysis to fit raw experimental data comprising the mROR curve to the governing equations (equations (9) and (10), respectively). The regression fitting parameters are A and B, thus outputting K and r_{eff} for a given fluid, wick geometry, and porosity. Importantly, these methods do not involve any user decisions around data-scrubbing, fitting range, etc, because they use the entire mROR data sets.

In this work, the non-linear regression analysis was performed in MATLAB using the *lsqcurvefit* function and the Levenberg–Marquardt algorithm. Here, the user only needs to supply an initial guess for parameters A and B, and the code optimizes for minimum deviation between the developed best-fit curve and measured mROR curve. The resulting fit equations are plotted in figures 11(a) and (b) for the *t–m* and *m–t* approaches, respectively. Although the procedure of both methods is nearly identical, there are nuances in the fitting processes that differentiate them. In particular, the slope of the *t–m* curve approaches infinity as time increases, whereas it approaches zero for the *m–t* curve. For the former, regression convergence is not always guaranteed, and a trial-and-error approach is required for the initial A and B selection. Added to this, there is non-negligible sensitivity of prediction accuracy for the initial guess of A and B. Finally, even for the best solution (which was found iteratively here), there is nearly 10% error when compared with the ideal hypothetical curve; a comparison is shown in figure 11(a). Conversely, the *m–t* method achieved almost zero error in both A and B parameters, and this was insensitive to initial input.

A positive feature of both the *t–m* and *m–t* methods is that they do not require initial smoothing and/or secondary curve-fitting of the measured data, as required in the dm/dt method, for example. In order to assess the potential for data scatter (normal in measured data sets) to influence the prediction accuracy, random noise was added to the originally continuous hypothetical wick data using the superposition of the MATLAB *stairs* function and the *rand* function with an amplitude

Table 3. Comparison between all mROR models.

	Performance factors			
	Data preprocessing[a]	Fitting range	Convergence[b]	Associated error
Lucas–Washburn model	Not needed	Very sensitive	Possible	Major
Gravity-based (dm/dt) model	Mandatory	Very sensitive	Possible	Major
Gravity-based (t–m) model	Not needed	Entire data set	Possible with reasonable initial guess	Minimal
Gravity-based (m–t) model	Not needed	Entire data set	Not sensitive to the initial guess	Minimal

Excellent
Good
Fair

[a] Data preprocessing refers to the cleaning and smoothing step.
[b] For the first and second model, the convergence means reaching high R^2.

of 0.0000 25 g. The resulting 'noisy' data plots are shown in figures 11(c) and (d), along with the best fit regression curves. It was found that both methods achieved errors identical to that of the original noiseless curve, indicating robustness in the approaches.

Table 3 compares each mROR method with respect to key factors, such as data cleaning/scrubbing steps, fitting range, convergence, and the associated error. The gravity-based m–t method is clearly the best choice for predicting wick properties from mROR experiments and is thus the method used hereafter.

4.2. Effect of immersion length

To the best of our knowledge, the influence of immersion length, l, has not been reported in previous studies. It has been generally reported that the wick sample must be lowered sufficiently to contact the liquid; however, the immersion depth has not been quantified, presumably because it was difficult to determine due to experimental apparatus limitations and/or the meniscus attachment event. This is not the case with the present facility, where the sample motion is precisely controlled and the moment of liquid contact is sensed, giving a precise zeroing with respect to the liquid surface. It was then possible to test a range of immersion lengths to explore to what extent these impact mROR curve repeatability and the subsequent level of error on wick parameter estimation.

Figure 12(a) shows the raw mROR data for Wick 1 for immersion lengths in the range 0.0 mm $\leqslant l \leqslant$ 2.1 mm. Prior to each run, the wick was dried using a hot plate and allowed to cool to ambient temperature. Additionally, the liquid level was maintained constant between the runs. It can be observed that for increased immersion length, the mass gain (Δm_g) that occurs when the sample is lifted (here at t =300 s) decreases. This occurs because the scale measures the net mass, which is the summation of the mass decrease by the weight of the immersed part of the wick as the sample is lifted upward and the mass increase by the meniscus detachment (Δm_0). Thus, $\Delta m_g = \Delta m$ only for zero immersion length.

Figure 12 shows the mROR curves after applying the corrections listed in section 3.5. To illustrate the error associated with not controlling or quantifying the immersion depth, it is assumed that $\Delta m_g = \Delta m$ even for non-zero immersion lengths. Clearly, as the immersion length is increased, the mROR curves shift upwards owing to the incorrect estimation of the meniscus mass. Although the effect may appear small, table 4 indicates that the influence on the A and B parameter estimation is non-negligible. For a l = 1.1 mm immersion depth, the error is around 7% and 3% for A and B respectively, and these propagate onto the error of the wick permeability and effective pore radius estimation; thus, they should either be included as a source of measurement uncertainty or eliminated altogether by the method proposed here to ensure zero immersion depth. An additional benefit to actively controlling the wick position using the electrical resistance method is its excellent repeatability; figure 12(c) shows nearly identical mROR curves for three independent tests on Wick 1.

4.3. Off-the-shelf wick characterization

To illustrate the overall functionality and precision and error estimation capabilities of the proposed measurement facility, the commercial wicks prepared in section 3.1 were tested with the zero-immersion depth method, and the wick parameters were estimated using the gravity-based m–t method. Figure 13 shows the mROR curves for each sample wick with ethanol as the working fluid. For each wick, the rise velocity is initially high due to the negligible gravity effects, and this lasts for a few seconds. Then, the velocity slows due to the opposing influences of both frictional resistance and the hydrostatic pressure of the absorbed liquid. The curves plateau when the capillary pressure is balanced (primarily by hydrostatic pressure). The noticeable difference in mass uptake between the different wick samples is largely due to differences in wicks.

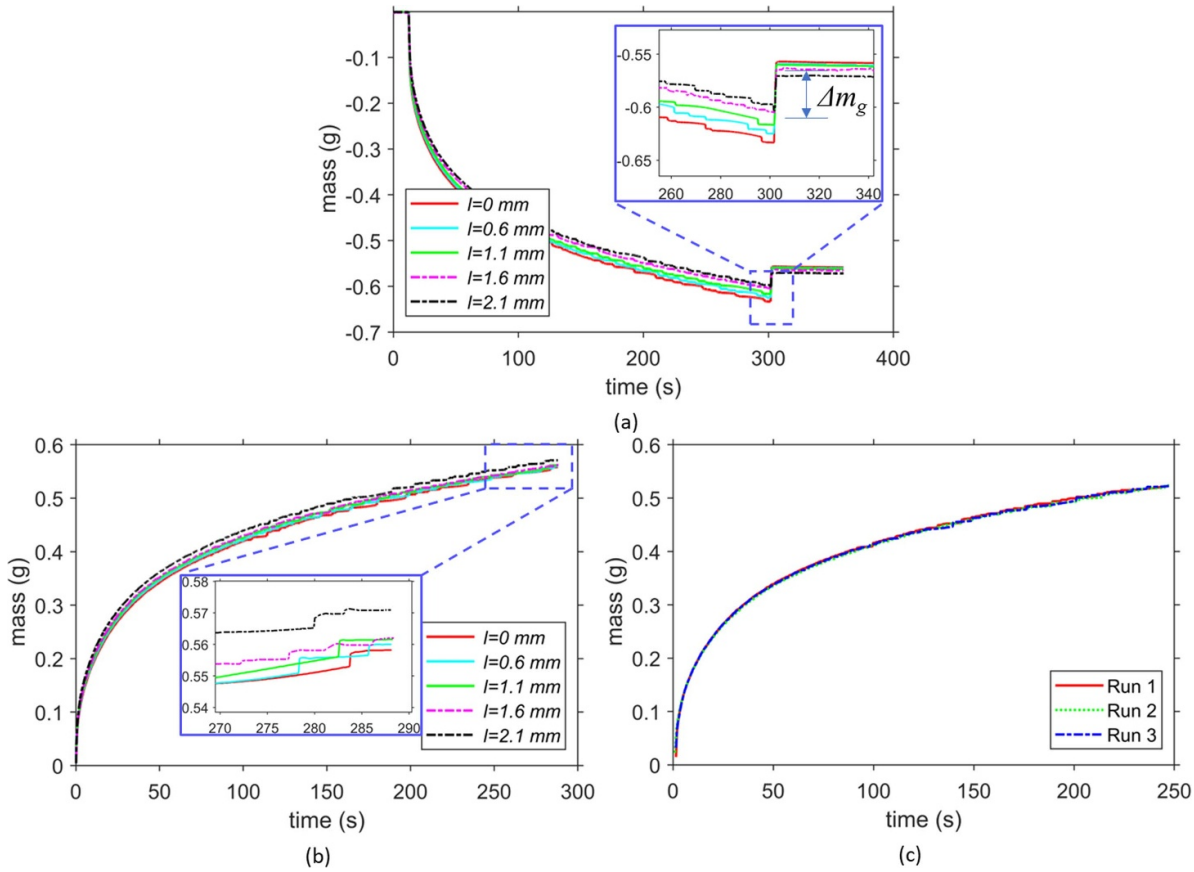

Figure 12. The effect of the immersion length: (a) raw mass data, (b) mass data after correction, and (c) repeatability of three independent tests.

Table 4. Influence of immersion depth on parameters A and B.

Immersion length, l (mm)	A (kg^2 s^{-1}) $\times 10^{-9}$	B (kg s^{-1})	$\frac{\lvert A_l - A_0\rvert}{A_0}$ x 100%	$\frac{\lvert B_l - B_0\rvert}{B_0}$ x 100%
0.0	1.92	3.37×10^{-6}	0.0%	0.0%
0.6	1.98	3.34×10^{-6}	3.1%	0.9%
1.1	2.05	3.47×10^{-6}	6.8%	3.0%
1.6	2.10	3.55×10^{-6}	9.4%	5.3%
2.1	2.25	3.78×10^{-6}	17.2%	12.2%

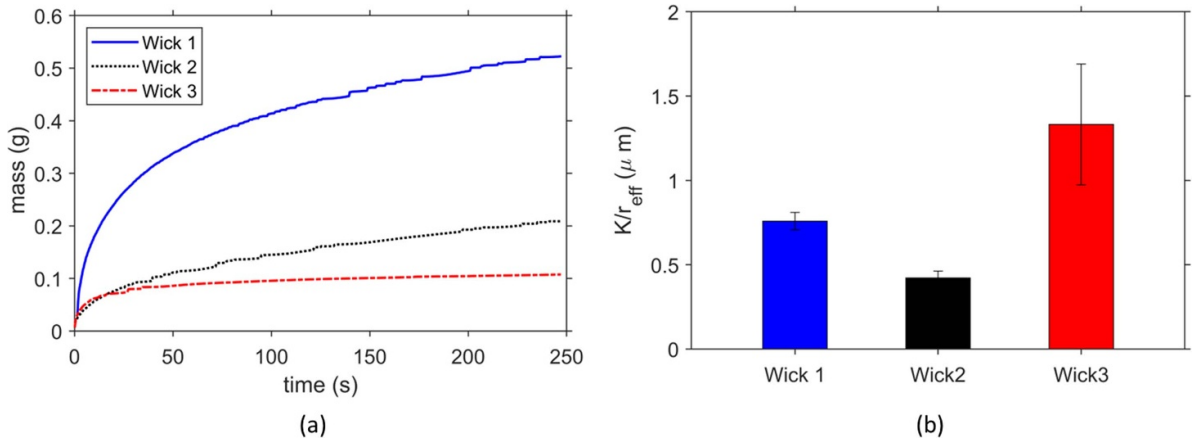

Figure 13. Comparison of the wicks in terms of (a) mass measurement and (b) the permeability/effective radius ratio.

Table 5. Measured wick parameters.

Sample ID	A ($kg^2\ s^{-1}$) $\times 10^{-9}$	$(\omega_{m-t})_A$ ($kg^2\ s^{-1}$) $\times 10^{-12}$	$(\omega_{\Delta t_o})_A$ ($kg^2\ s^{-1}$) $\times 10^{-12}$	B ($kg\ s^{-1}$) $\times 10^{-6}$	$(\omega_{m-t})_B$ ($kg\ s^{-1}$) $\times 10^{-9}$	$(\omega_{\Delta t_o})_B$ ($kg\ s^{-1}$) $\times 10^{-8}$	Porosity, ε (–)		ω_ε (–)
							h–t	*XCT*	
Wick 1	1.92	3.04 (0.16%)	40.8 (2.12%)	3.37	7.65 (0.23%)	9.55 (2.12%)	0.59	0.62	0.014
Wick 2	0.15	0.72 (0.49%)	3.21 (2.15%)	0.42	5.60 (1.31%)	2.11 (4.94%)	0.58	0.61	0.019
Wick 3	0.229	2.10 (0.91%)	7.94 (3.46%)	2.22	22.4 (1.01%)	8.19 (3.69%)	0.61	0.59	0.041

Table 6. Capillary performance parameters of the tested commercial wick samples.

Sample ID	K (μm^2)	ω_K (%)	R_{eff} (μm)	$\omega_{R_{eff}}$ (%)	K/R_{eff} (μm)	$\omega_{K/R_{eff}}$ (%)
Wick 1	48.03	3.37	63.4	5.9	0.757	6.81
Wick 2	16.14	5.48	38.26	7.84	0.4217	9.57
Wick 3	123.24	10.97	92.53	24.53	1.33	26.8

Wick 1, for example, shows the highest wicking capacity due its larger width and thickness (see table 2).

The *m–t* method (discussed in section 4.1) was then applied for each mROR curve to extract the wick parameters A and B, which are given in table 5. This table also includes the porosity measurement results using the *m–t–h–t* method (discussed in section 3.4). Also shown are the measured porosities obtained using the XCT measurements technique; these show sufficient agreement to verify the accuracy of the straightforward *m–t–h–t* method. As such, the *m–t–h–t* measurement for porosity was used to exemplify that the proposed facility can be used as an all-in-one measurement device for porosity, permeability, and effective pore radius.

The uncertainties listed in table 5 were predicted by propagating the mass uncertainty (± 0.0012 g) and the time delay error, Δt_0, through the fitting algorithm, as explained in section 3.6. The uncertainty in both parameters (A and B) resulting from the scale error, (ω_{m-t}), is not significant compared with the compounded error originating from the delay time $(\omega_{\Delta t_0})$. This is due to the high accuracy of the analytical balance used and the use of the *m–t* method which demonstrates low sensitivity to random noise in the data (see section 4.1).

Table 6 shows the key wick property and uncertainty results for each commercial wick tested. Figure 13(b) also lists and plots the ratio K/r_{eff} because it is a more physical assessment of the wick capillary performance; this is because it is proportional to the maximum capillary pumping power of conventional heat pipes [31]. It can be noted that much larger uncertainty was determined for Wick 3; this is due primarily to the relative non-uniformity wick cross-section observed in this wick (see figure 2). This wick also produces the highest K/r_{eff}, followed by Wick 1 and Wick 2, in turn. This illustrates that, despite similar porosity, sintered copper wicks can perform quite differently, depending on internal morphology. This of course is a function of the wick fabrication process including, but not limited to, powder size and sintering temperature and pressure. Notably, despite having the highest effective pore radius, Wick 3 has a disproportionately higher permeability compared with the other two, thus making it a higher performance wick.

5. Conclusion

This paper presents a new mROR test facility and analysis method for measuring wick porosity, permeability, and effective pore radius. The key findings of this work are as follows:

- The Lucas–Washburn, dm/dt, and t–m methods of parameter estimation are inadequate and the *m–t* method is suggested as the most appropriate analysis model for extracting wick properties from experimental mROR data.
- A robust uncertainty analysis has been developed which propagates experimental error to the extent that the error of measured permeability and effective pore radius can be estimated; to the best of our knowledge, this is a first in this field of measurement.
- The depth to which wicks are immersed in the liquid has been shown to cause non-negligible error on the measured wick parameters, and a method to ensure zero immersion depth is detailed and implemented.
- Three commercial sintered copper wicks from different flat heat pipe manufacturers were tested. The results show that the quality of the wick can influence the estimated error on the measured wick parameters, particularly if the geometry is not uniform.
- Of the three commercial wicks tested, one outperformed the other two, illustrating that not only can the current test facility confidently quantify relevant wick parameters to differentiate between seemingly similar wicks, but the internal structure and morphology of sintered copper wicks is crucial for performance in heat pipe applications.

Data availability statement

The data that support the findings of this study are available upon reasonable request from the authors.

Acknowledgments

The authors gratefully acknowledge the support of the Ontario Centre of Innovation (OCI).

ORCID iDs

J Durfee https://orcid.org/0000-0002-8708-9276
J P Mooney https://orcid.org/0000-0001-8787-7160
R Kempers https://orcid.org/0000-0001-5927-8726

References

[1] Adkins D R and Dykhuizen R C 1993 Procedures for measuring the properties of heat-pipe wick materials *Proc. Intersociety Energy Conversion Engineering Conf.* vol 2 pp 911–7
[2] Holley B and Faghri A 2006 Permeability and effective pore radius measurements for heat pipe and fuel cell applications *Appl. Therm. Eng.* **26** 448–62
[3] Li Q, Lan Z, Chun J, Lian S, Wen R and Ma X 2021 Fabrication and capillary characterization of multi-scale micro-grooved wicks with sintered copper powder *Int. Commun. Heat Mass transfer* **121** 105123
[4] Zhang S, Chen C, Chen G, Sun Y, Tang Y and Wang Z 2020 Capillary performance characterization of porous sintered stainless steel powder wicks for stainless steel heat pipes *Int. Commun. Heat Mass transfer* **116** 104702
[5] Deng D, Tang Y, Huang G, Lu L and Yuan D 2013 Characterization of capillary performance of composite wicks for two-phase heat transfer devices *Int. J. Heat Mass Transfer* **56** 283–93
[6] Lucas R 1918 Ueber das Zeitgesetz des kapillaren Aufstiegs von Flüssigkeiten *Kolloidn. Z* **23** 15–22
[7] Gardner W 1921 The dynamics of capillary flow *Phys. Rev.* **18** 206–9
[8] Shirazy M R S and Fréchette L G 2013 Capillary and wetting properties of copper metal foams in the presence of evaporation and sintered walls *Int. J. Heat Mass Transfer* **58** 282–91
[9] Fries N and Dreyer M 2008 An analytic solution of capillary rise restrained by gravity *J. Colloid Interface Sci.* **320** 259–63
[10] Rogacs A, Steinbrenner J E, Rowlette J A, Weisse J M, Zheng X L and Goodson K E 2010 Characterization of the wettability of thin nanostructured films in the presence of evaporation *J. Colloid Interface Sci.* **349** 354–60
[11] Zhang S, Lin L, Chen G, Tang H, Zeng J, Yuan W and Tang Y 2019 Experimental study on the capillary performance of aluminum micro-grooved wicks with reentrant cavity array *Int. J. Heat Mass Transfer* **139** 917–27
[12] Deng D, Liang D, Tang Y, Peng J, Han X and Pan M 2013 Evaluation of capillary performance of sintered porous wicks for loop heat pipe *Exp. Therm. Fluids Sci.* **50** 1–9
[13] Jafari D, Wits W W and Geurts B J 2018 Metal 3D-printed wick structures for heat pipe application: capillary performance analysis *Appl. Therm. Eng.* **143** 403–14
[14] Li H, Fu S, Li G, Fu T, Zhou R, Tang Y, Tang B, Deng Y and Zhou G 2018 Effect of fabrication parameters on capillary pumping performance of multi-scale composite porous wicks for loop heat pipe *Appl. Therm. Eng.* **143** 621–9
[15] Maneemuang S, Vafai K, Kammuang-Lue N, Terdtoon P and Sakulchangsatjatai P 2021 Analysis of the optimum configuration for the capillary rise and the permeability of the fiber wick structure for heat removal in heat pipes *Heat Mass Transfer* **57** 1513–26
[16] Wong S-C, Deng M-S and Liu M-C 2022 Characterization of composite mesh-groove wick and its performance in a visualizable flat-plate heat pipe *Int. J. Heat Mass Transfer* **184** 122259
[17] Fries N, Odic K, Conrath M and Dreyer M 2008 The effect of evaporation on the wicking of liquids into a metallic weave *J. Colloid Interface Sci.* **321** 118–29
[18] Feng C, Yugeswaran S and Chandra S 2018 Capillary rise of liquids in thermally sprayed porous copper wicks *Exp. Therm. Fluids Sci.* **98** 206–16
[19] Lu L, Sun J, Liu Q, Liu X and Tang Y 2017 Influence of electrochemical deposition parameters on capillary performance of a rectangular grooved wick with a porous layer *Int. J. Heat Mass Transfer* **109** 737–45
[20] Tang Y, Tang H, Li J, Zhang S, Zhuang B and Sun Y 2017 Experimental investigation of capillary force in a novel sintered copper mesh wick for ultra-thin heat pipes *Appl. Therm. Eng.* **115** 1020–30
[21] Tang Y, Deng D, Lu L, Pan M and Wang Q 2010 Experimental investigation on capillary force of composite wick structure by IR thermal imaging camera *Exp. Therm. Fluids Sci.* **34** 190–6
[22] Barry D A, Parlange J-Y, Li L, Prommer H, Cunningham C J and Stagnitti F 2000 Analytical approximations for real values of the Lambert W-function *Math. Comput. Simul.* **53** 95–103
[23] du Plessis A, Broeckhoven C, Guelpa A and le Roux S G 2017 Laboratory x-ray micro-computed tomography: a user guideline for biological samples *Gigascience* **6** 1–11
[24] Ziółkowski G, Chlebus E, Szymczyk P and Kurzac J 2014 Application of x-ray CT method for discontinuity and porosity detection in 316L stainless steel parts produced with SLM technology *Arch. Civ. Mech. Eng.* **14** 608–14
[25] Backeberg N R, Iacoviello F, Rittner M, Mitchell T M, Jones A P, Day R, Wheeler J, Shearing P R, Vermeesch P and Striolo A 2017 Quantifying the anisotropy and tortuosity of permeable pathways in clay-rich mudstones using models based on x-ray tomography *Sci. Rep.* **7** 1–12
[26] Heim K, Bernier F, Pelletier R and Lefebvre L-P 2016 High resolution pore size analysis in metallic powders by x-ray tomography *Case Stud. Nondestruct. Test. Eval.* **6** 45–52
[27] Gobert C, Kudzal A, Sietins J, Mock C, Sun J and McWilliams B 2020 Porosity segmentation in x-ray computed tomography scans of metal additively manufactured specimens with machine learning *Addit. Manuf.* **36** 101460
[28] Kruth J P, Bartscher M, Carmignato S, Schmitt R, De Chiffre L and Weckenmann A 2011 Computed tomography for dimensional metrology *CIRP Ann.—Manuf. Technol.* **60** 821–42
[29] Maire E and Withers P J 2014 Quantitative x-ray tomography *Int. Mater. Rev.* **59** 1–43
[30] Object Research Systems Inc. n.d. *Dragonfly | 3D Visualization and Analysis Solutions for Scientific and Industrial Data | ORS* D.O.I. 2018 (available at: https://theobjects.com/dragonfly/index.html) (Accessed 19 August 2022)
[31] Štorkánová H *et al* 2021 3D printed aluminum flat heat pipes with micro grooves for efficient thermal management of high power LEDs *Sci. Rep.* **11** 1–8